Catal Lett (2012) 142:936–945
DOI 10.1007/s10562-012-0845-x

Mixed Lanthana/Ceria Nanorod-Supported Gold Catalysts for Water–Gas-Shift

Shuang Liang · Götz Veser

Received: 24 February 2012 / Accepted: 10 May 2012 / Published online: 2 June 2012

Abstract We report on the preparation of $La_xCe_{1-x}O_y$ nanorods (x = 0−0.5) with uniform aspect ratio, and their evaluation as active supports for Au in the water–gas shift (WGS) reaction. By independently controlling aspect ratio and composition, we demonstrate that the reducibility of the nanorods is determined by the preferential exposure of highly active {110} planes and the La:Ce ratio. After deposition of Au onto these nanorods, the WGS activity is closely correlated with the reducibility of the oxides, indicating that the strong relationship between activity and reducibility previously reported for nanoparticle-based catalysts holds independent of morphology.

Keywords Water–gas shift · Cerium oxide · Lanthanum oxide · Gold · Nanostructure

1 Introduction

Oxide-supported metal catalysts are widely used across a broad range of applications, including fuel processing, environmental protection, and the production of fine chemicals [1–3]. Recent advances in materials chemistry have strongly revived this field by allowing for unprecedented control over size, shape, and composition of materials from the molecular scale up, thus giving insights into the relationship between activity/selectivity and the composition/structure of oxide-supported metal catalysts with the promise to find next-generation materials with strongly improved catalytic properties [3–7].

Oxide-supported Au catalysts, in particular, have been studied extensively since Haruta et al. [8] discovered the exceptional activity of Au nanoparticles for low temperature CO oxidation [9]. Recently, Flytzani-Stephanopoulos and coworkers [10–12] demonstrated high activity of Au/metal oxide catalysts for water–gas shift (WGS), making them promising alternatives to commercial Cu-based and Fe-based catalysts, which suffer from insufficient stability and poor low-temperature activity. However, the oxidation state and particle size for the active Au species in these catalysts are still extensively debated and investigated [12–15]. Significantly, however, it is well established that in these catalysts, beyond the active Au species, the oxide support plays an important role in the rate-determining H_2O dissociation step for WGS [16–18]. In particular CeO_2 is considered as one of the most effective supports for Au catalysts as the facile conversion between Ce^{4+} and Ce^{3+} on the oxide surface allows cerium oxide to act as oxygen storage and oxygen transfer material in redox reactions [6, 19].

To improve the activity of ceria, several strategies have been widely pursued, such as compositional and structural tailoring. On one hand, doping of ceria has been shown to result in improved performance in WGS due to increased reducibility and oxygen storage capacity [19–26]. On the other hand, several research groups have recently shown that nanostructuring can also significantly affect the redox activity of pure ceria [5–7, 27, 28]. Especially CeO_2 nanorods show superior activity compared to (polyhedral) nanoparticles in CO oxidation and in WGS [6, 7, 29, 30].

S. Liang · G. Veser
US DOE-National Energy Technology Laboratory, Pittsburgh, PA, USA

S. Liang · G. Veser (✉)
Department of Chemical Engineering, University of Pittsburgh, 1249 Benedum Hall, Pittsburgh, PA 15261, USA
e-mail: gveser@pitt.edu

However, to-date, only very few studies have focused on doped ceria with well-defined nanostructures, i.e. on the combined effect of simultaneous structural and compositional tailoring [27, 31, 32]. In particular, no reports exist to-date on mixed $La_xCe_{1-x}O_y$ nanorods as catalyst support for WGS, despite the above mentioned findings that both La-doping and nanostructuring into rod shapes results in significantly enhanced WGS activity.

The main target of the present study was therefore to develop a better understanding of the function of rare earth additives (here: La) in the redox properties and WGS activity of CeO_2 nanorods. Highly homogenous mixed $La_xCe_{1-x}O_y$ nanorods were synthesized over a broad range of La content (0–50 %) via a carefully controlled hydrothermal synthesis. After depositing Au onto these nanorods—while carefully controlling for uniform metal loading, surface area and particle aspect ratio—these catalyst were evaluated in WGS, and showed superior activity compared to analogous nanoparticle catalysts. However, unlike for nanoparticle catalysts, we find that La doping does not yield improved WGS activity for nanorod-based catalysts.

2 Experimental Section

2.1 Materials and Syntheses

$Au/La_xCe_{1-x}O_y$ catalysts were prepared via a two-step synthesis. First, the oxide supports with controlled morphologies were synthesized via hydrothermal or microemulsion methods, followed by Au loading via deposition–precipitation (DP).

CeO_2 and $La_xCe_{1-x}O_y$ nanorods were prepared by hydrothermal synthesis. For example, to prepare $La_{0.5}Ce_{0.5}O_{1.75}$ nanorods, 0.376 g of $La(NO_3)_3{\cdot}6H_2O$ (99+ %, Sigma-Aldrich) and 0.376 g of $Ce(NO_3)_3{\cdot}6H_2O$ (99+ %, Sigma-Aldrich) were dissolved in 8 ml DI water. 30 ml of NaOH (98+ %, Sigma-Aldrich) solution (3.5 M) was rapidly added under vigorous stirring. After 30 min of stirring, the slurry was transferred into a 50 ml autoclave, heated to 100 °C under autogenous pressure for 72 h, and then allowed to cool to room temperature. The product was washed by DI water and collected via centrifugation to remove any ionic remnants until the pH of the solution was seven. After drying at 100 °C overnight and calcination at 450 °C for 4 h, the final product was obtained.

Pure CeO_2 nanoparticles were prepared through hydrolysis of cerium isopropoxide in a reverse (water-in-oil) microemulsion, as previously reported by our group [19, 33]. The microemulsion was composed of water, isooctane (2,2,4-trimethylpentane, 99.7 % Aldrich), poly(ethylene glycol)-*block*-poly(propylene glycol)-*block*-poly(ethylene glycol) (Aldrich, Mn = 2000) and 1-pentanol (99+ %, Aldrich). The Ce-isopropoxide in isopropanol was added to the microemulsion, and the solution was aged for 70 h under constant stirring at room temperature. After phase separation, the gel was washed in acetone four times, freeze-dried, and finally calcined at 450 °C for 4 h.

All $Au/La_xCe_{1-x}O_y$ catalysts were prepared from the respective oxide nanostructures via deposition–precipitation (DP) [34]. $HAuCl_4$ (99.9+ %, Aldrich) solution was added drop-wise at room temperature into an aqueous slurry of the oxide, keeping the pH of the slurry fixed at pH = 8.0 via addition of 0.2 M $(NH_4)_2CO_3$ (93.5+ %, J.T.Baker). The resulting precipitate was aged at room temperature for 1 h, filtered, washed, dried at 100 °C, and then calcined at 400 °C for 2 h. The nominal Au loading for all catalysts was 5 wt%.

2.2 Characterization

The specific surface area was determined via nitrogen sorption in a Micromeritics ASAP 2020 gas adsorption analyzer using the BET method. Prior to the measurement, the samples were degassed for 2 h at 200 °C under high vacuum. Elemental analysis to determine Au loading and La/Ce ratio were performed using inductively coupled plasma optical emission spectroscopy (ICP-OES) on a Thermo iCAP 6500 spectrometer, and using energy-dispersive X-ray analysis (EDX) equipped on transmission electron microscopy (JEOL-2100F). The EDX analysis is based on the microdomains of nanorods under TEM. The X-ray diffraction (XRD) measurements were performed with a high-resolution powder X-ray diffractometer (Bruker AXS D8) in line focus mode employing Cu–Kα radiation (λ = 1.5406 Å). Crystal phases were identified based on JCPDS cards. Sample morphology was determined by transmission electron microscopy (JEOL-200CX, JEOL-2100F). Lattice spacings were calculated by fast Fourier transformation (FFT) analysis of the high resolution TEM images. Temperature-programmed reduction by hydrogen (H_2-TPR) was conducted using a Micromeritics Chemisorb 2750 system equipped with a thermal conductivity detector. During the TPR analysis, the samples were first oxidized in 5 vol.% O_2/He at 450 °C for 2 h, and then TPR was performed by heating the sample (100 mg) at 5 °C/min to 900 °C in a 10 vol.% H_2/Ar flow (30 ml/min). A cold trap filled with acetone-dry ice mixture was placed between reactor and TCD to remove water vapor.

2.3 Catalyst Tests

Water–gas shift tests were carried out in a 5 mm ID quartz glass tube heated via insertion into a high-temperature tube furnace at ambient pressure. The catalyst powder (50 mg)

was supported within the tube on either end by quartz glass felt plugs. Water was injected via a syringe pump and vaporized in a heated line before entering the reactor. The composition of the mixture after water addition was 10.8 % H_2O, 2.1 % CO, and 87.1 % He. The total flow rate of gas was typically around 100 CCM resulting in space velocities of $\sim$150,000 h^{-1}. The exit gas passed through a condenser to eliminate H_2O from the stream and then was analyzed by an Agilent 3000A MicroGC equipped with thermal conductivity detector (TCD). In order to assure reaching steady state after adjusting operating conditions (such as temperature steps), CO conversion was measured repeatedly until the conversion varied less than 1 % over a duration of 5 min. No methane was detected at any conditions used in this work. The inert helium feed was used as internal standard to calculate the total gas flow rate after water condensation and the concentration of water leaving the reactor.

3 Results and Discussion

3.1 Nanorod Morphology

As shown in Fig. 1a, pure CeO_2 samples prepared via hydrothermal synthesis (and after calcination at 450 °C) form nanorods. Previous studies have demonstrated superior catalytic activity for such ceria nanorods and explained this due to preferential exposure of highly reactive crystal planes [6, 28, 35, 36]: CeO_2 nanoparticles with face-centered cubic crystal structure mostly expose {111} planes, which are thermodynamically most stable and least reducible [6, 19, 26]. In contrast to that, HR-TEM (Fig. 1b) shows that nanorods expose preferentially {110} orientations: Fast Fourier transformation (FFT) analysis of the two-dimensional crystal lattice image of a nanorod with a growth axis perpendicular to the electron beam yields a lattice parameter of 3.13948 Å, in close agreement with the {111} plane spacing (3.1250 Å) of cubic CeO_2 (JCPDS 34-0394). Based on the measured interplanar spacings and the plane-intersecting angle, we can hence identify {111} planes and the exposed active {110} side planes of the rod, confirming previous results [6, 7].

In order to take advantage of the superior activity of nanorods for mixed oxide materials, and to ascertain that any difference obtained in the present investigation can be correlated with composition rather than change in aspect ratio of the sample, it is necessary to control the synthesis of $La_xCe_{1-x}O_y$ to yield the same rod-shape morphology. However, as shown in Fig. 1b–d, the $La_xCe_{1-x}O_y$ samples obtained from 24 h hydrothermal synthesis (i.e. identical conditions as for CeO_2 nanorod synthesis), contain incompletely formed nanorods and nanoparticles. Figure 2 (left) summarizes the results and shows that the aspect ratio of mixed-oxide nanorods drops from 8.3 to 2.9 with increasing La content from 0–50 %, indicating that the La dopant inhibits the growth of ceria along the [110] direction.

In order to obtain well-defined nanorods with preferential exposure of {110} planes, the duration of the hydrothermal synthesis was extended to allow for complete formation of the final structure. Figure 2 (right) shows the aspect ratio of $La_{0.5}Ce_{0.5}O_{1.75}$ as a function of synthesis duration, illustrating the growth of mixed lanthana/ceria nanorods over a 72 h period (3 days). After 72 h hydrothermal reaction, the $La_xCe_{1-x}O_y$ exhibit uniform rod-shape structures (Fig. 1f–h) with similar average aspect ratios of 7.38–8.14 (Table 1), comparable to that of pure CeO_2 nanorods (8.3). Correspondingly, all nanorod materials also have similar surface areas of 84–99 m^2/g (Table 1). Thus, the controlled synthesis of the $La_xCe_{1-x}O_y$ nanorods allows de-coupling of structural and compositional effects on the activity of the catalysts, and the high aspect-ratio nanorods were consequently used in the reducibility and WGS activity tests.

The compositional homogeneity of the mixed oxide nanorod was confirmed via XRD, high resolution TEM, and microdomain EDX. Figure 3 shows the XRD patterns of $La_xCe_{1-x}O_y$ nanorods prepared by hydrothermal synthesis after calcination at 450 °C. The sharp diffraction peaks in Fig. 3a are in a good agreement with the CeO_2 standard (JCPDS 34-0394). The XRD diffractograms of all $La_xCe_{1-x}O_y$ exhibit a shifted fluoride crystal structure without the presence of second phase, such as La_2O_3, (Fig. 3b–d), indicating the formation of homogenous mixed oxides in which La^{3+} ions are embedded into the cubic crystal lattice of CeO_2. The lattice parameters of $La_xCe_{1-x}O_y$ nanorods calculated from these diffraction patterns are in a good agreement with theoretical values reported by Morris et al. [37] (see Table 1) as well as with our previously reported observations for $La_xCe_{1-x}O_y$ nanoparticles, despite the significant differences in the materials morphologies [26]. This is further confirmed via high resolution TEM (Fig. 4), where the lattice spacing of $La_xCe_{1-x}O_y$ was directly determined via FFT analysis of the images, as shown in Fig. 4. As the La loading ("x") increases from 0 to 0.5, the lattice spacing of (111) expands from 3.13948 to 3.36638 Å. This lattice expansion can be attributed to a combination of the larger ionic radius of La^{3+} versus Ce^{4+} and the effect of the increasing number of oxygen vacancies due to La doping [37, 38]. Finally, EDX analysis of microdomains of the samples showed uniform La:Ce ratios in good agreement with the expected values from the synthesis (see Table 3).

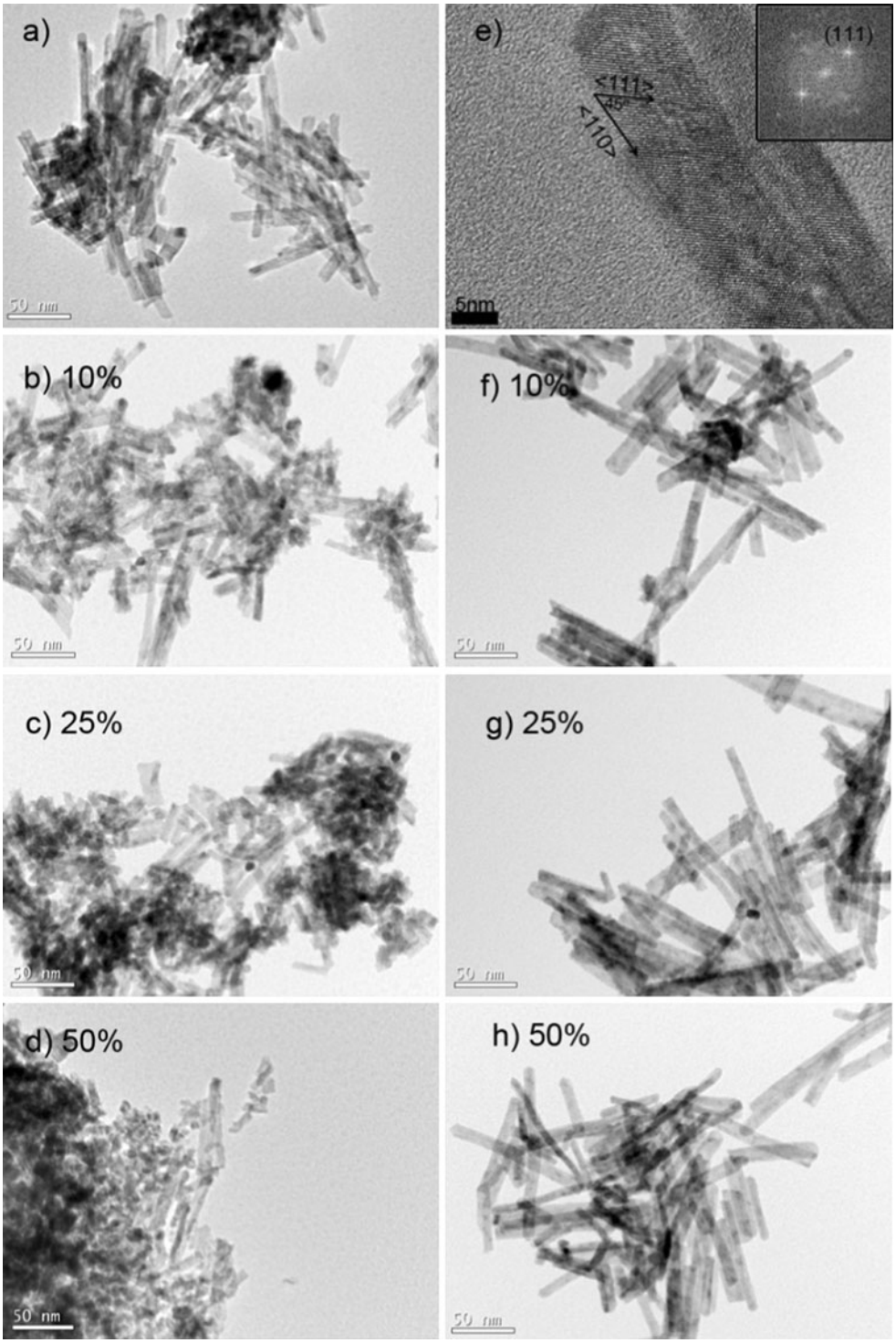

Fig. 1 TEM (**a**) and HR-TEM (**e**) images of CeO_2 nanorods. TEM images of nanorods with different La contents (%) prepared by 24 h hydrothermal synthesis (**b–d**); and by 72 h hydrothermal synthesis (**f–h**), respectively

3.2 Reducibility of $La_xCe_{1-x}O_y$

In order to evaluate the redox properties of these materials, temperature-programmed reduction in hydrogen (H_2-TPR) has been used extensively in the literature [6]. Active metals, such as Au and Cu, show low activity for H_2O dissociation, which is the rate determining step for WGS [16, 17]. In comparison, ceria has no reported WGS activity but is active in water dissociation due to the presence of reduced Ce^{3+} sites [16]. Based on this

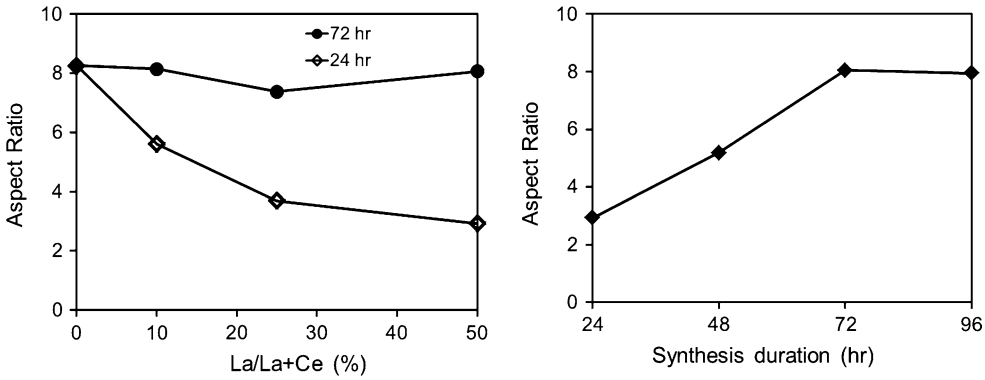

Fig. 2 *Left* average aspect ratio of $La_xCe_{1-x}O_y$ as function of La content (0–50 %) after 24 h (*open symbols*) and 72 h (*filled symbols*) synthesis time, respectively. *Right* average aspect ratio of $La_{0.5}Ce_{0.5}O_{1.75}$ nanorods as function of synthesis duration

Table 1 Theoretical and experimental value of the pure and mixed-oxide nanorods' lattice parameter, surface area and aspect ratio

	Lattice parameter (Å)			BET surface area (m^2/g)	Average aspect ratio
	Theoretical	Experimental NR	Experimental NP		
CeO_2	5.3950	5.4239	5.4250	99.0	8.3
$La_{0.1}Ce_{0.9}O_{1.95}$	N.A.*	5.4484	5.4644	91.2	8.1
$La_{0.25}Ce_{0.75}O_{1.875}$	5.4820	5.4942	5.4966	84.6	7.4
$La_{0.5}Ce_{0.5}O_{1.75}$	5.5720	5.5832	5.5702	87.8	8.1

* The lattice parameter of $La_{0.1}Ce_{0.9}O_{1.95}$ was not reported in the Ref. [37]

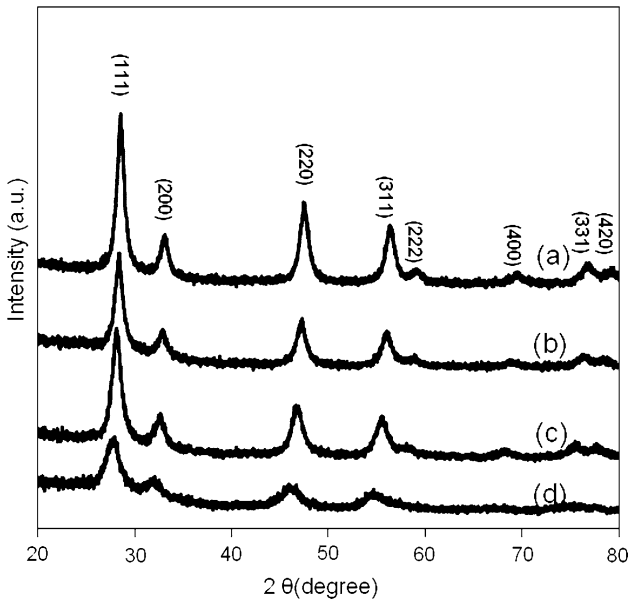

Fig. 3 X-ray diffraction patterns of $La_xCe_{1-x}O_y$ nanorod materials with different lanthanum content: (*a*) 0 %, (*b*) 10 %, (*c*) 25 %, (*d*) 50 % (percent is mol% metal, i.e. La/(Ce + La))

mechanism, the reducibility of oxide supports can be expected to have a strong impact to the catalytic WGS activity of Au/$La_xCe_{1-x}O_y$ catalysts.

Figure 5 shows the TPR profile for pure and mixed oxide samples. For pure CeO_2 nanoparticles, two reduction peaks are visible, one at low temperature (~420 °C) and one at high temperature (>700 °C, not fully shown in the graph), which can be attributed to the reduction of surface and of bulk ceria, respectively [39, 40]. Only the low-temperature surface reduction is relevant in the present context, since it occurs in the temperature range of interest for WGS (T < 500 °C). In comparison, CeO_2 nanorods have a lower reduction temperature (360 vs. 420 °C) and a much higher H_2 consumption (781 vs. 396 μmol/g; calculated from an integration of the area under the curves), indicating a much higher overall reducibility. This can be traced back to the preferential exposure of active {110} crystal planes as discussed previously.

Remarkably, doping CeO_2 nanorods with La does not significantly improve the reducibility of the nanorods. As shown in Fig. 5, the onset temperature for the reduction of the three samples with 0, 10, and 25 % La doping is unchanged (~180 °C), and the peak reduction temperature shows only a minor shift by ~15 °C upon La doping. When the La content is increased to 50 %, however, a strong increase in the onset temperature for reduction to 220 °C is observed and a strongly increased reduction peak temperature of ~420 °C are observed, indicating that a higher La content is in fact detrimental to the reducibility of the mixed oxide nanorods.

Beyond the change in reduction temperatures, the area under the reduction peak, representing the total amount of reducible sites (quantified in the specific hydrogen consumption values in Table 2), shows a more obvious and pronounced trend towards lower values with increasing La content for all mixed-oxide nanorods. This decrease in H_2 consumption indicates a loss in reducible sites with

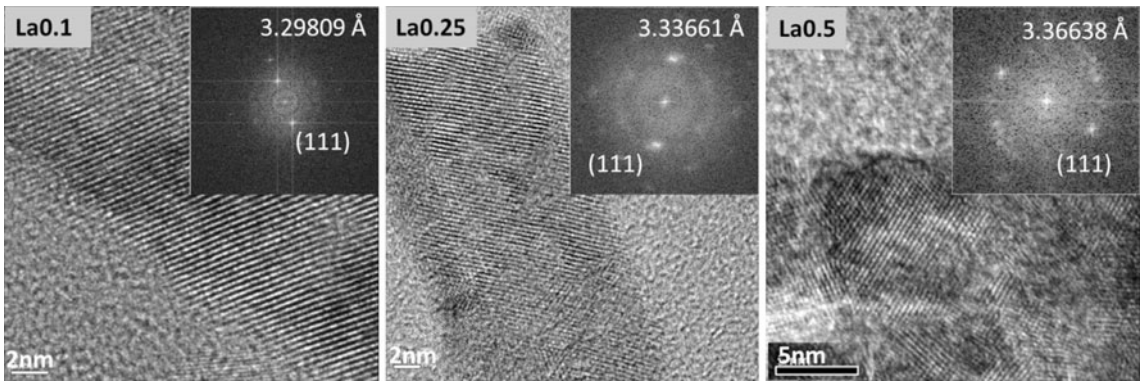

Fig. 4 HR-TEM and FFT analysis (inserted) of $La_xCe_{1-x}O_y$ with x = 0.1, 0.25, and 0.5

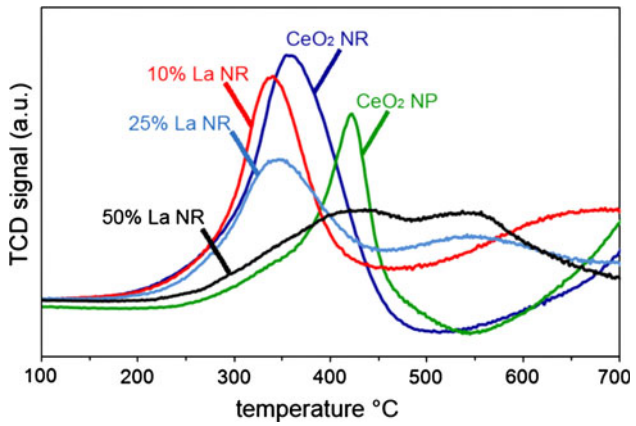

Fig. 5 H_2-TPR profiles of $La_xCe_{1-x}O_y$ nanorods with different La content (10–50 %), ceria nanorods (NR) and nanoparticles (NP)

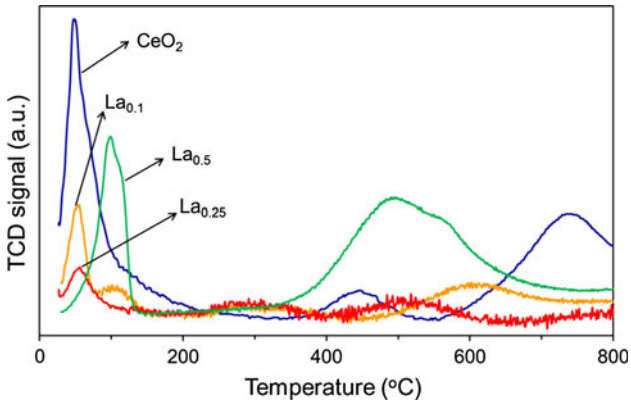

Fig. 6 H_2-TPR profiles of Au/$La_xCe_{1-x}O_y$ nanorods with different La content (10–50 %)

Table 2 Reduction temperature and hydrogen consumption

	Reduction temperature (°C)	H_2 consumption (μmol H_2/g oxide)
CeO_2 (NP)	420	396
CeO_2 (NR)	355	781
$La_{0.1}Ce_{0.9}O_{1.95}$	340	461
$La_{0.25}Ce_{0.75}O_{1.875}$	345	388
$La_{0.5}Ce_{0.5}O_{1.75}$	420	336

increasing La doping which can be explained by the substitution of reducible Ce^{4+} by La^{3+}, which is much less reducible in this low-temperature range. (Pure La_2O_3—not shown in the figure—has very low reducibility with a TPR peak at ~430 °C and a H_2 consumption in TPR of 88 vs. 396 μmol/g for CeO_2 nanoparticles, as reported previously [26]) Interestingly, this result differs from our previous investigation of mixed Ce/La-oxide nanoparticles where La dopings up to ~25 % (i.e. up to $La_{0.25}Ce_{0.75}O_{1.875}$) resulted in a strong increase in reducible sites compared to pure CeO_2 nanoparticles [19, 26]. A possible explanation for this discrepancy can be found in the different reducibility of the terminal planes for the different nanostructures: for nanoparticles, which are terminated predominantly by {111} planes, the La doping facilitates the conversion of Ce^{4+}/Ce^{3+} in and near the {111} planes, thus creating defects in the oxygen sub-lattice, enhancing the oxygen mobility, and hence increasing the overall reducibility of the mixed oxide nanoparticles [26]. In contrast to that, the dopant cannot further "activate" the terminal {110} planes in the nanorods, which already have a much lower formation energy for defects than the {111} planes [6, 36]. Doping hence results only in the above described decrease in the number of reducible oxygen sites, and hence a decrease in reducibility. While we were not able to prepare well-defined nanorods with La-content >50 % due to the inhibiting effect of La on CeO_2 nanorod growth, it can hence be expected based on the trends observed here that higher La-content nanorods will have even lower reducibility.

The reducibility of $La_xCe_{1-x}O_y$ is strongly affected by the Au deposition, as shown in Fig. 6. The most important change is that a new reduction peak at very low temperature (~100 °C) appears for Au/$La_xCe_{1-x}O_y$, which has

been attributed to the reduction of oxidized Au species [11, 41–43] or to reduction of the oxide via hydrogen spill-over from the metal to the support [44–46]. Since the surface reduction peaks for all oxide supports are significantly decreased after Au deposition, it indicates that most available oxygen is reduced at this lower temperature, and thus suggests that H_2 dissociation on Au and spill-over onto the adjacent oxide surface are more likely to be responsible for the strong low-temperature reduction peak.

The trend in the reducibility of the Au-based catalysts is in close agreement with that of the oxide supports (Fig. 5): $Au/La_xCe_{1-x}O_y$ nanorods have very similar reduction temperatures up to $x = 0.25$, whereas the sample with 50 % La shows a significantly higher reduction temperature. Furthermore, Au/CeO_2 shows the highest reduction peak, indicating that lanthanum replaces reducible Ce^{4+}, and hence decreases the reducibility of these catalysts. (We currently have no consistent explanation for the apparent increase in number of reducible sites from $x = 0.25$ to 0.5.)

Overall, these results hence confirm our previous report that La doping results in two counter-acting effects [26]: On one hand, it increases the reducibility of the samples by lowering the reduction energy and the activation energy for oxygen migration in CeO_2; on the other hand, it decreases the reducibility by reducing the absolute number of reducible Ce^{4+}. For 10 and 25 % La, the balance of the two effects causes a slightly lower reduction peak with similar onset temperature and less reducible sites. However, when the La doping is increased to 50 %, the second effect becomes dominant, resulting in a net loss of reducibility of the sample. (It should be noted here that the broad peaks at 500–600 °C for $La_{0.25}Ce_{0.75}O_{1.875}$ and $La_{0.5}Ce_{0.5}O_{1.75}$ in Fig. 5 are not due to sample reduction, but due to decomposition of surface carbonates. La_2O_3 is well known to form surface hydroxy-carbonates, $La_2(OH)_4(CO_3)$, when exposed to air, which decompose to $La_2O_2CO_3$ and further to La_2O_3 in this temperature range [47, 48].)

Table 3 Measured Au loading and La content of $Au/La_xCe_{1-x}O_y$

	Au wt%	Average particle size of Au	La/(La + Ce) (from EDX)
Au/CeO_2 (NP)	3.8	<3 nm*	0
Au/CeO_2 (NR)	3.9	2.8	0
$Au/La_{0.1}Ce_{0.9}O_{1.95}$	4.1	2.5	0.11
$Au/La_{0.25}Ce_{0.75}O_{1.875}$	3.8	2.6	0.25
$Au/La_{0.5}Ce_{0.5}O_{1.75}$	4.1	2.6	0.49

*As reported previously, the Au particle size on CeO_2 nanoparticles is <3 nm. However, it was not possible to determine the exact Au particle size on CeO_2 nanoparticle supports via TEM or chemisorptions due to their similar contrast and chemisorption properties [19]

3.3 WGS Activity

In order to further identify composition-activity correlations, Au/mixed oxide WGS catalysts were prepared via deposition–precipitation of Au onto $La_xCe_{1-x}O_y$ nanorods with near-identical aspect ratios. Elemental analysis after deposition–precipitation (DP) of Au (Table 3) confirms Au loadings of ~4 wt% for all samples, and La contents in close agreement with the expected values. As shown in the TEM and HAADF-STEM images in Fig. 7, $La_xCe_{1-x}O_y$ nanorods maintained their morphology and dimensions during the DP process. Particle sizes and size distributions determined from bright-field and dark-field images show good agreement with average Au particle sizes of ~2.6–2.8 nm and fairly narrow particle size distributions (see inserted bar graphs in Fig. 7). While there is an on-going debate in the literature over the oxidation state [12, 14] and size [49, 50] of the active Au species in WGS catalysis, the present investigation did not aim to contribute to this discussion, but rather focus solely on the role of the oxide support. However, by following identical and carefully controlled deposition–precipitation and pretreatment methods, and assuring identical Au loadings, particle sizes,

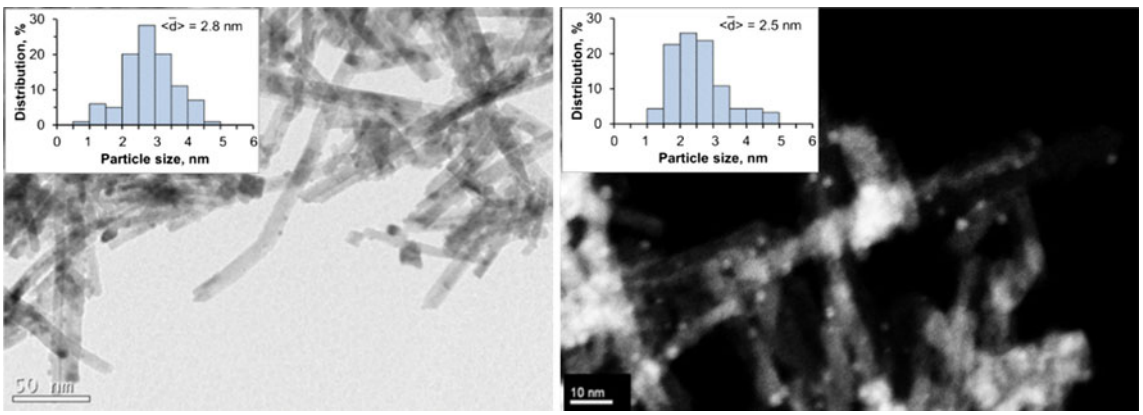

Fig. 7 TEM of Au/CeO_2 (*left*) and HAADF-STEM of $Au/La_{0.25}Ce_{0.75}O_{1.875}$ (*right*). The insets show the Au nanoparticle distributions determined from respective TEM images

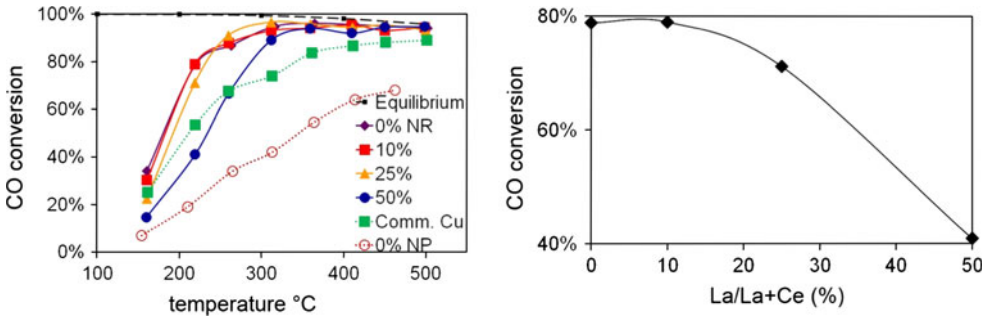

Fig. 8 *Left graph* CO conversion vs temperature in WGS for Au/$La_xCe_{1-x}O_y$ nanorods (NR) with different La content (0–50 %), Au/CeO_2 (0 % NP) and commercial Cu-based WGS catalyst ("Comm. Cu"). *Right graph* CO conversion (as measure of catalytic WGS activity) of Au/$La_xCe_{1-x}O_y$ NR as function of La content at a fixed temperature of 220 °C

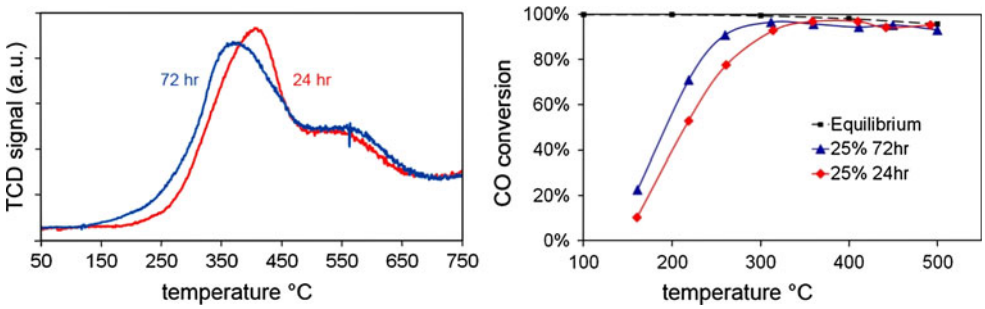

Fig. 9 *Left* H_2-TPR profiles of $La_{0.25}Ce_{0.75}O_{1.875}$ nanorods. *Right* CO conversion versus temperature in WGS for Au/$La_{0.25}Ce_{0.75}O_{1.825}$ nanorods synthesized with different hydrothermal durations

and distribution on the different catalysts, all catalysts should have the same number and type of active Au sites, and hence the difference in performance of the Au/$La_xCe_{1-x}O_y$ catalysts can be expected to be entirely due to the difference in the oxide supports.

The WGS activity of Au/$La_xCe_{1-x}O_y$ was tested in fixed-bed reactor studies feeding a mix of 10.8 % H_2O and 2.1 % CO in He into a 5 mm ID quartz-glass tube at a space velocity of ~150,000 h^{-1} (see experimental section for details). Figure 8 summarizes the results for Au/$La_xCe_{1-x}O_y$ samples, ranging from pure CeO_2 to 50 % La-content nanorod supports, in terms of CO conversion as function of temperature. For comparison, Au/CeO_2 nanoparticle catalysts (prepared via a microemulsion-templated synthesis) and a commercial Cu-based WGS catalyst (HiFUEL W220, Alfa Aesar) were included in the tests.

The most striking feature in the figure is the much higher activity of the nanorod-based catalysts in comparison to the Au/CeO_2 nanoparticle catalyst, with the best nanorod-based catalysts reaching equilibrium conversions at experimental conditions at temperatures as low as ~270 °C. This high activity of the nanorod catalysts correlates well with the reducibility data, i.e. the lower reduction temperature and larger number of reducible sites discussed above, and is in agreement with previous reports [7, 35]. It is worthwhile to notice the Au/CeO_2 nanorod catalysts show excellent low-temperature WGS activity even compared to the commercial Cu-based catalyst.

La doping has very little impact on this high WGS activity up to a La content of 25 %, while a further increase to 50 % La results in a significant drop in activity, in particular in the temperature range below ~350 °C. This again closely mirrors the trends seen in the reducibility of the samples, where an increase of La content from 25 to 50 % results in a strong loss of reducibility as well as the increase of reduction temperature (see Figs. 5, 6). This can be more clearly seen in the right-hand plot in Fig. 8, where CO conversion is shown as a function of La content for one fixed reaction temperature (T = 220 °C). Comparing the CO conversion curves (Fig. 8) with the reducibility trend (Figs. 5, 6 and Table 2), it is apparent that both activity and reducibility closely follow the same trend with La content of the Au/$La_xCe_{1-x}O_y$ nanorods.

Finally, the impact of aspect ratio on reducibility and WGS activity was studied separately by comparing $La_{0.25}Ce_{0.75}O_{1.875}$ nanorods obtained at different synthesis durations (24 and 72 h). As discussed before, the aspect ratio of $La_xCe_{1-x}O_y$, which determines the preferential exposure of the active {110} crystal plane, increases as the hydrothermal synthesis is extended up to 72 h.

As expected from the increased exposure of {110} planes, the high aspect-ratio nanorods (i.e. after 72 h synthesis time) show slightly improved reducibility, especially in the low temperature range <400 °C, with reduction starting at 110 °C, i.e. ~70 °C lower than for the low aspect-ratio sample (Fig. 9, left graph). Furthermore, the WGS activity of

the catalysts shows excellent agreement with this difference in reducibility between the nanorods: As shown in Fig. 9 (right), the high aspect-ratio Au/$La_{0.25}Ce_{0.75}O_{1.875}$ (i.e. after Au loading) shows 10 $\sim$ 20 % higher CO conversion at low temperature (<350 °C) than the low aspect-ratio sample. These differences thus demonstrate again the significance of establishing firm morphological control for these catalysts, and confirm the strong and direct correlation between reducibility and activity of Au/ceria-based WGS catalysts.

4 Summary

We demonstrated the synthesis of CeO_2 and, for the first time, mixed $La_xCe_{1-x}O_y$ nanorods via a simple hydrothermal reaction at high concentration of NaOH and without surfactant. The La doping was found to act as an inhibiter for the growth of $La_xCe_{1-x}O_y$ nanorods along the [110] direction. However, by controlling the hydrothermal duration, $La_xCe_{1-x}O_y$ nanorods with high aspect ratio and surface area could be synthesized with aspect ratio comparable to those previously reported pure CeO_2 nanorods. The use of these carefully controlled pure and mixed nanorods as supports for (equally uniform) Au nanoparticles allowed study of whether previous correlations between reducibility and activity for nanoparticle-based Au/mixed oxide catalysts are transferrable to nanorod catalysts.

In agreement with earlier reports, we found that the difference in reducibility between nanoparticles and nanorods can be attributed to preferential exposure of different terminal crystal planes. The preferential exposure of {110} crystal planes for CeO_2 nanorods results in lower reduction temperature and an increased number of reducible sites in the temperature range of WGS, resulting in strongly increased WGS activity compared to nanoparticle-based Au/ceria catalysts. However, unlike for nanoparticle-based catalysts, the reducibility of CeO_2 nanorods cannot be enhanced significantly by La doping, suggesting that the already low reduction energy of Ce^{4+} along the {110} planes cannot be further decreased by La. As a result, the WGS activity of pure Au/CeO_2 and Au/$La_xCe_{1-x}O_y$ with $x \leq 25$ % is essentially unchanged, with conversions significantly above those both for Au/ceria nanoparticle catalysts and a commercial Cu-based catalyst. Further increase in La content results in decreased activity due to the decrease in reducible oxygen sites.

The present study hence confirms that the strong relationship between catalyst reducibility and WGS catalytic activity holds independent of the morphology of the oxide support, i.e. it is applicable both to CeO_2 nanoparticle and nanorod-based catalysts.

References

1. Matatov-Meytal YI, Sheintuch M (1998) Ind Eng Chem Res 37:309
2. Khodakov AY, Chu W, Fongarland P (2007) Chem Rev (Washington, DC, U. S.) 107: 1692
3. Haruta M (1997) Catal Today 36:153
4. Yi N, Si R, Saltsburg H, Flytzani-Stephanopoulos M (2010) Appl Catal B 95:87
5. Mai H-X, Sun L-D, Zhang Y-W, Si R, Feng W, Zhang H-P, Liu H-C, Yan C-H (2005) J Phys Chem B 109:24380
6. Zhou K, Wang X, Sun X, Peng Q, Li Y (2005) J Catal 229:206
7. Si R, Flytzani-Stephanopoulos M (2008) Angew Chem Int Ed 47:2884
8. Haruta M, Yamada N, Kobayashi T, Iijima S (1989) J Catal 115:301
9. Hashmi ASK, Hutchings GJ (2006) Angew Chem Int Ed 45:7896
10. Fu Q, Weber A, Flytzani-Stephanopoulos M (2001) Catal Lett 77:87
11. Fu Q, Kudriavtseva S, Saltsburg H, Flytzani-Stephanopoulos M (2003) Chem Eng J 93:41
12. Fu Q, Saltsburg H, Flytzani-Stephanopoulos M (2003) Science 301:935
13. Deng W, Frenkel AI, Si R, Flytzani-Stephanopoulos M (2008) J Phys Chem C 112:12834
14. Daly H, Goguet A, Hardacre C, Meunier FC, Pilasombat R, Thompsett D (2010) J Catal 273:257
15. Rodriguez J, Wang X, Liu P, Wen W, Hanson J, Hrbek J, Pérez M, Evans J (2007) Top Catal 44:73
16. Senanayake SD, Stacchiola D, Evans J, Estrella M, Barrio L, Perez M, Hrbek J, Rodriguez JA (2010) J Catal 271:392
17. Liu P (2010) J Chem Phys 133:204705
18. Rodriguez J, Ma S, Liu P, Hrbek J, Evans J, Perez M (2007) Science 318:1757
19. Wang Y, Liang S, Cao A, Thompson RL, Veser G (2010) Appl Catal B 99:89
20. Balducci G, Islam MS, Kaspar J, Fornasiero P, Graziani M (2000) Chem Mater 12:677
21. Ilieva L, Pantaleo G, Ivanov I, Nedyalkova R, Venezia AM, Andreeva D (2008) Catal Today 139:168
22. Ho CM, Yu JC, Wang XC, Lai SY, Qiu YF (2005) J Mater Chem 15:2193
23. Di Monte R, Kaspar J (2005) J Mater Chem 15:633
24. Rao GR, Kašpar J, Meriani S, Monte R, Graziani M (1994) Catal Lett 24:107
25. de Leitenburg C, Trovarelli A, Llorca J, Cavani F, Bini G (1996) Appl Catal A 139:161
26. Liang S, Broitman E, Wang Y, Cao A, Veser G (2011) J Mater Sci 46:2928
27. Lin K-S, Chowdhury S (2010) Int J Mol Sci 11:3226
28. Zhang F, Jin Q, Chan SW (2004) J Appl Phys 95:4319
29. Niu F, Zhang D, Shi L, He X, Li H, Mai H, Yan T (2009) Mater Lett 63:2132
30. Huang Y, Pemberton JE (2010) Colloids Surf A 360:175
31. Lang J, Han Q, Yang J, Li C, Li X, Yang L, Zhang Y, Gao M, Wang D, Cao J ((2010)) J Appl Phys 107:074302
32. Yang Y, Wang X, Sun C, Li L (2010) J Am Ceram Soc 93:2555
33. Kirchhoff M, Specht U, Veser G (2005) Nanotechnology 16:S401
34. Fu Q, Weber A, Flytzani-Stephanopoulos M (2001) Catal Lett 77:87
35. Lin F, Hoang D, Tsung C-K, Huang W, Lo S, Wood J, Wang H, Tang J, Yang P (2011) Nano Res 4:61
36. Sayle DC, Maicaneanu SA, Watson GW (2002) J Am Chem Soc 124:11429

37. Morris BC, Flavell WR, Mackrodt WC, Morris MA (1993) J Mater Chem 3:1007
38. Patil S, Seal S, Guo Y, Schulte A, Norwood J (2006) Appl Phys Lett 88:243110
39. Huang X-S, Sun H, Wang L-C, Liu Y-M, Fan K-N, Cao Y (2009) Appl Catal B 90:224
40. Yuan Q, Duan H-H, Li L-L, Sun L-D, Zhang Y-W, Yan C-H (2009) J Colloid Interface Sci 335:151
41. Andreeva D, Idakiev V, Tabakova T, Ilieva L, Falaras P, Bourlinos A, Travlos A (2002) Catal Today 72:51
42. Sandoval A, Gomez-Cortes A, Zanella R, Diaz G, Saniger J (2007) J Mol Catal A Chem 278:200
43. Idakiev V, Tabakova T, Naydenov A, Yuan Z, Su B (2006) Appl Catal B 63:178
44. Boccuzzi F, Chiorino A, Manzoli M, Andreeva D, Tabakova T (1999) J Catal 188:176
45. Collins S, Cies J, del Rio E, Lopez-Haro M, Trasobares S, Calvino J, Pintado J, Bernal S (2007) J Phys Chem C 111:14371
46. Jacobs G, Ricote S, Patterson PM, Graham UM, Dozier A, Khalid S, Rhodus E, Davis BH (2005) Appl Catal A 292:229
47. Bernal S, Botana FJ, García R, Rodríguez-Izquierdo JM (1987) React Solid 4:23
48. Klingenberg B, Vannice MA (1996) Chem Mater 8:2755
49. Herzing AA, Kiely CJ, Carley AF, Landon P, Hutchings GJ (2008) Science 321:1331
50. Hua J, Zheng Q, Zheng Y, Wei K, Lin X (2005) Catal Lett 102:99